# Letters

# Passive Intermodulation Source Localization Based on Emission Source Microscopy

Shaohui Yong , Student Member, IEEE, Sen Yang , Student Member, IEEE, Ling Zhang , Student Member, IEEE, Xiong Chen, Student Member, IEEE, David J. Pommerenke , Fellow, IEEE, and Victor Khilkevich, Member, IEEE

Abstract—Emission source microscopy (ESM) technique can be used for localization and characterization of electromagnetic interference sources by measuring the magnitude and phase of the electromagnetic field in the far-field zone. This article presents a method which uses ESM to locate sources of passive intermodulation (PIM). Compared to the traditional methods of PIM source localization techniques including mechanical manipulation of potential sources and near-field scanning, the proposed ESM-based approach does not require access to the devices under test allowing to detect the PIM sources at relatively large distances. Moreover, the influence of background PIM generated by surrounding environment can be reduced by ESM focusing. The high-quality maps of reconstructed PIM sources can be obtained by using ESM. The feasibility of manual sparse ESM scanning, which is more practical in realistic settings is also demonstrated.

*Index Terms*—Base station antennas, emission source microscopy (ESM), passive intermodulation (PIM).

#### I. INTRODUCTION

ASSIVE intermodulation (PIM) is a spectrum noise problem that is caused by nonlinearity of passive components. Some mechanisms of PIM generation have been presented in the previous articles [1]–[3]. PIM is usually caused by nonlinear components and effects (e.g., diodes, nonideal metal contacts, saturation of the permeability of metals). In modern wireless communication systems, multiple high-power signals having different frequencies often share the same base station antenna and due to the PIM their intermodulation products might fall into the receiver's band, compromising its sensitivity [4]–[6]. Locating radiated PIM sources has become a critical issue for engineers.

A traditional method for PIM source localization is to manipulate or remove all possible components manually until the PIM source is identified, which is very time consuming and costly. Another approach is near-field scanning [7]–[9]. The localization of the PIM sources is determined by moving a probe to identify the locations having the largest field strength at the PIM frequency. However, near-field probes are practically unable to reach close enough to all locations and components on complex devices under test (DUT), which leads to uncertainties of

Manuscript received December 4, 2018; revised April 15, 2019 and July 15, 2019; accepted August 28, 2019. Date of publication September 18, 2019; date of current version February 13, 2020. (*Corresponding author: Shaohui Yong.*)

- S. Yong is with the Electrical Engineering, EMC Laboratory, Missouri University of Science and Technology, Rolla, MO 65409 USA (e-mail: sy2m5@mst.edu).
- L. Zhang and X. Chen are with the EMC Laboratory of Missouri S&T, Rolla, MO 65409 USA (e-mail: lzd76@mst.edu; chenxio@mst.edu).
- S. Yang, D. J. Pommerenke, and V. Khilkevich are with the Electrical Engineering, Missouri University of Science & Technology, Rolla, MO 65409 USA (e-mail: sydgf@mst.edu; david.pommerenke@ieee.org; khilkevichv@mst.edu).

Color versions of one or more of the figures in this article are available online at http://ieeexplore.ieee.org.

Digital Object Identifier 10.1109/TEMC.2019.2938634

source localization. Nowadays, the time-domain reflectometry-based radiated PIM source characterization methods [10]–[12] are widely adopted in PIM analyzers. In one implementation this approach fixes the frequency of one carrier signal and sweeps the other carrier over the entire available bandwidth. The inverse fast Fourier transform is performed on the reflected PIM signal to reconstruct a time-domain pulse. The timing of the pulse can be used to estimate the distance to the PIM source. However, the PIM analyzers inevitably have very limited operational bandwidth determined by the duplexers inside the PIM analyzer. Furthermore, the operation frequency (usually below 3 GHz) is relatively low which results in a long wavelength, causing poor resolution which is often in the order of meters according to the manufacturers' specifications.

Emission source microscopy (ESM) is a technique that can localize and characterize radiation sources of a complex system by measuring the field magnitude and phase over planar surface a few wavelengths away from the DUT, and back-propagating the scanned field onto the DUT [13]–[15]. ESM allows to detect the radiation sources (including sources of PIM) at relatively large distances, which is suitable for complex or concealed DUT. This article presents a new approach to locate PIM radiation sources using ESM technique. The measurement system and properties of the methodology are discussed.

## II. OVERVIEW OF ESM TECHNIQUE

The ESM algorithm is based on the synthetic aperture radar technique, which uses the two-dimensional (2-D) Fourier transformation. The field (image) on the DUT plane after back-propagation can be expressed as follows [13]:

$$E_t^0(x, y, 0) = \mathcal{F}^{-1} \left\{ \mathcal{F} \left[ E_t(x, y, z_0) \right] \cdot e^{jk_z z_0} \right\}$$
 (1)

where  $E_t(x,y,z_0)$  is the tangential fields on the scanning planar surface. Reverse and forward two-dimensional (2-D) spatial Fourier transform operators are  $\mathcal{F}^{-1}$  and  $\mathcal{F}$ . The distance between the scanning and imaging plane is  $z_0$ , and  $k_z$  is the z component of the propagation vector, which is related to the wave number  $k_0$  and spatial frequencies  $k_x$  and  $k_y$  as  $k_z = \sqrt{k_0^2 - k_x^2 - k_y^2}$ .

An advantage of the proposed PIM localization method is that the out-of-focus PIM signals reflected or generated by the surrounding environment or the probe itself will be reduced by the focusing process.

To illustrate the impact of ESM focusing, a test is performed by using two log-periodic antennas set on planes with different heights and fed by the same signal generated by a vector network analyzer (VNA). The antenna at the zero distance along the z axis represents the ambient noise source, and the antenna at 0.5 m height—the radiating DUT to be localized. The measurement is performed by moving another log-periodic antenna connected to the second port of the VNA, on the

0018-9375 © 2019 IEEE. Personal use is permitted, but republication/redistribution requires IEEE permission. See https://www.ieee.org/publications/rights/index.html for more information.

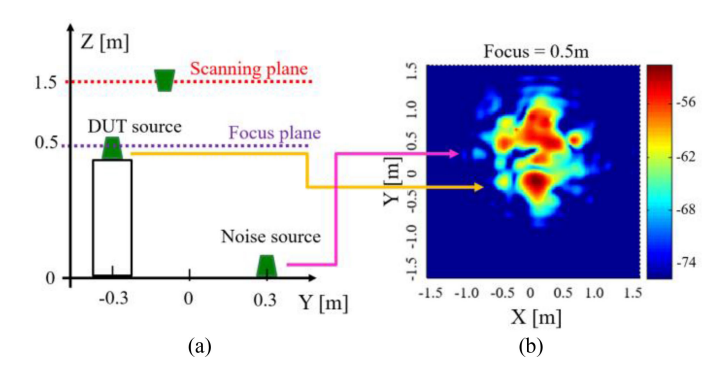


Fig. 1. (a) Two log-periodic antennas are fed by the same signal at 1 GHz generated by the VNA and equally separated by a power divider. (b) Reconstructed E-field magnitude in dBV/m of two sources when focusing to the plane 0.5 m above the floor. The distance between the scanning plane and the DUT source is about three times of the wavelength.

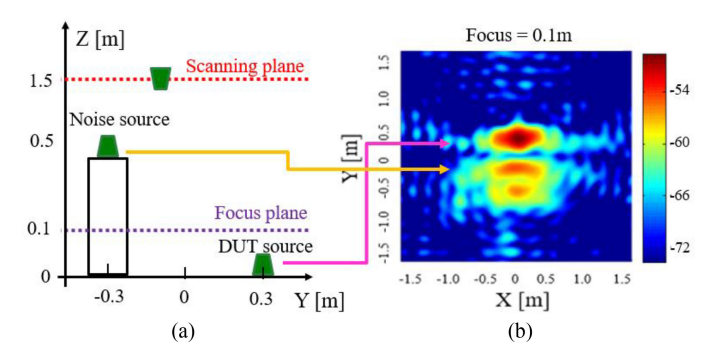


Fig. 2. (a) Two log-periodic antennas are fed by the same signal at 1 GHz generated by the VNA and equally separated by a power divider. (b) Reconstructed E-field magnitude in dBV/m of two sources when focusing to the plane 0.1 m above the floor. The distance between the scanning plane and the DUT source is about five times of the wavelength.

plane at the height of 1.5 m and recording the value of the transmission coefficient  $S_{21}$  (the antenna positioning is performed by using the optical tracking system – see Section V for details). The largest dimensions of the dipole elements in the antennas is 13.4 cm which allows to estimate the far field-distance F of the antennas as 12 cm at 1 GHz (using  $F = 2D^2/\lambda$ , where D is the antenna dimension). The image is obtained by focusing the measured plane distribution to the DUT plane using (1). The corresponding image is shown in Fig. 1. The darkest red hotspot corresponding to the DUT source can be observed clearly. The noise source contributes to the image by the "cloud" in the top part of the plot. The peak value of the "cloud" is about 5 dB lower than the peak value of the DUT image, demonstrating suppression of out-of-focus sources by the ESM, allowing to identify dominating sources of EMI (or radiating PIM) despite the background noise.

In the second example the bottom antenna represents the DUT and the top one—the noise source; the focus plane is set to 0.1 m. As Fig. 2(b) shows, suppression for the peak value of out-of-focus source is again about 5 dBV/m.

#### III. SYSTEM SETUP

The system setup is illustrated in Fig. 3. By placing a DUT with nonlinear components in a relatively high-power electromagnetic field created by a low-PIM antenna (GSM base station antenna) connected to a low-PIM source (PIM analyzer), PIM noise is generated.

The carrier signals with frequencies  $f_1 = 1932.6$  MHz and  $f_2 = 1985.2$  MHz are generated by the PIM analyzer (CCI PIMPro 1921 [16]). The base station antenna used in this setup has a typical PIM

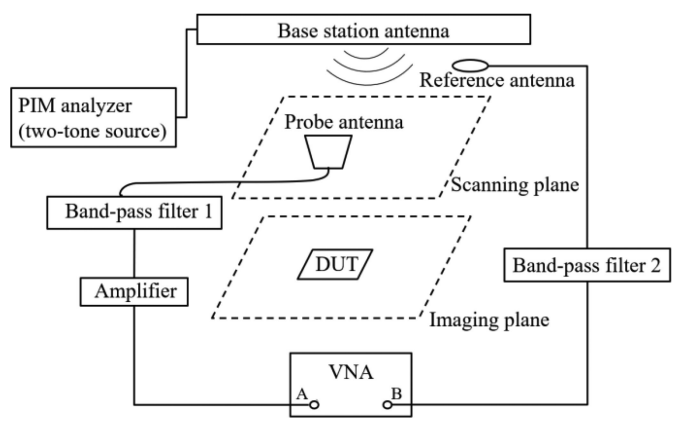


Fig. 3. Overview of the measurement setup.

level of  $-120\,\mathrm{dBm}$  across the working frequency, i.e., much lower than the anticipated PIM produced by the DUT. The Tx port of the PIM analyzer is connected to the base station antenna via a low-PIM cable.

To generate the PIM noise, several printed circuit boards (PCB) with nonlinear components are placed at a distance of about 70 cm away from the base station antenna. Another type of the PIM-generating DUT used in the study is a piece of copper wool, known to be a strong source of PIM due to numerous metal-oxide-metal junctions.

For ESM scanning, two probes/antennas are needed to measure the magnitude and phase data. One of the probes is used for scanning, and the other to obtain a phase reference as described in [14]. The scanning is carried out on a plane above the DUT using a log-periodic antenna with a frequency band 850–6500 MHz. To form a reference probe the inner and outer conductors of a coaxial cable were connected together (without soldering) to form a loop antenna loaded by a metal-oxidemetal junction, generating considerable PIM at the output of the coaxial cable. The reference probe is placed close to the base station antenna to obtain a strong reference signal. Signals from probe and reference antenna are fed into channels A and B of a VNA operating in the tuned receiver mode.

In order to determine the absolute value of the image on the DUT plane (allowing to measure the radiation intensity of the source for example), the actual field intensity on the scan plane needs to be measured. To achieve this, the VNA needs to be calibrated and the probe effect compensated. On the other hand, in the case when the calibration is omitted, and the back-scattering of the probe (reflections of the incident field between the probe and environment) is neglected. The scaling of the scan field by an arbitrary complex number (due to attenuation and phase shift in the measurement cables and the probe factor as well as multiple reflections in the receiving channels), will change the absolute values of the image, but it will not change the spatial distribution on the image plane as follows from (1) due to linearity of transformation from  $E_t(x, y, z_0)$  to  $E_t^0(x, y, 0)$ . As the aim of the article was to demonstrate feasibility of the PIM imaging and estimate the achievable resolution, the VNA calibration and probe compensation were not performed. Because of this all images presented below are scaled (by unknown numbers) relative to the actual distributions.

An important consideration for implementation of the ESM scanning system is the relative phase measurement accuracy. It is determined of course by the accuracy of the relative phase measurement in the VNA, which is, according to the specification of the VNA used in the test, is equal to  $\pm 0.5^{\circ}$ . A much larger contribution to the phase error is due to the accuracy of the probe positioning. The maximum phase uncertainty due to probe displacement  $\Delta x$  is equal to the total phase of the plane wave propagating in the direction  $\Delta x$ , which is

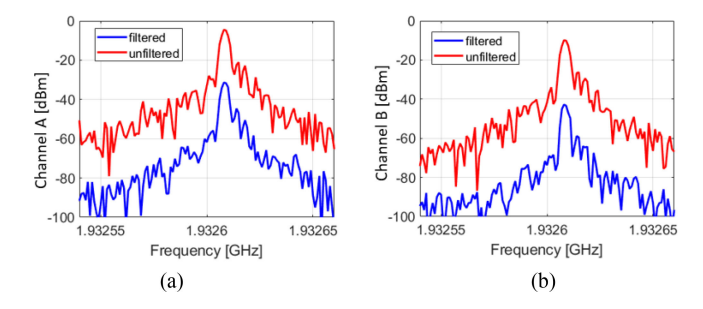


Fig. 4. Carrier signal on the (a) probe channel, and (b) reference channel at  $f_1=1932.6~\mathrm{MHz}.$ 

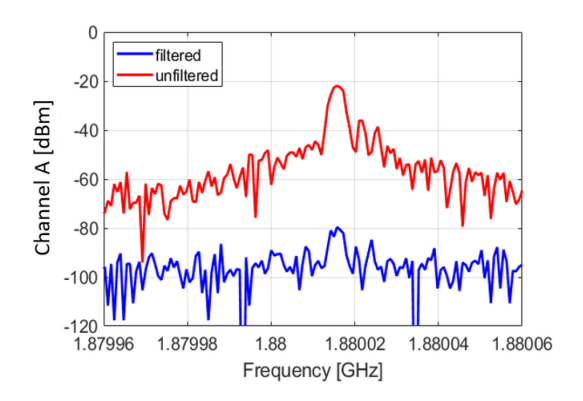


Fig. 5.  $f_{\rm PIM}=1880.0$  MHz. The measured signals with and without filtering on the probe channel at  $f_{\rm PIM}=1880.0$  MHz. The filters attenuate the PIM component by about 60 dB.

given by  $k_0\Delta x$ . The positioning accuracy for both methods used in the experiments (the robotic scanner and optical tracking system—see description below) is around 1 mm, leading to roughly 2.5° phase error at the PIM frequency (making the positioning accuracy a dominating factor in the phase uncertainty). As numerical experiments show, such small phase uncertainty does not lead to noticeable degradation of ESM images.

Proper filtering and amplification of the PIM signal is needed to avoid generating PIM in the measurement instrument. Two surface acoustic wave (SAW) band-pass filters are added in both probe channels to suppress the carrier signals. For our application with the carrier signal frequencies  $f_1=1932.6~{\rm MHz}$  and  $f_2=1985.2~{\rm MHz}$ , the PIM signal frequency is  $f_{\rm PIM}=2\cdot f_1-f_2=1880.0~{\rm MHz}$ . Two SAW band-pass filter with a center frequency of 1880 MHz and a bandwidth of 120 KHz are inserted into both channels to attenuate the carrier signals at  $f_1$  and  $f_2$ . To improve the signal-to-noise ratio (SNR) in the probe channel, a low noise amplifier, which can offer about 15 dB gain, is placed after the SAW band-pass filter. Because the reference antenna is placed very close to the base station antenna, the SNR in the reference channel was good enough and amplification was not necessary.

To test the SNR optimization performed using filters, the measurement of signals at carrier frequency  $(f_1 \text{ and } f_2)$  with and without the filters is performed on the VNA. No DUT is placed in the detection area, and the probe antenna is set at a distance of about 30 cm from the base station antenna. As Fig. 4 shows, the filters attenuate the carrier signals at  $f_1$  are attenuated by 27 and 33 dB in the probe and reference channel, respectively. The attenuation of the carrier signals at  $f_2$  is about 32 and 37 dB on the probe and reference channel. Such filtering leads to obvious improvement in the sensitivity at  $f_{\rm PIM}$ . As Fig. 5 shown, the signal at  $f_{\rm PIM}$  measured by the receiver is reduced to about  $-80~{\rm dBm}$ 

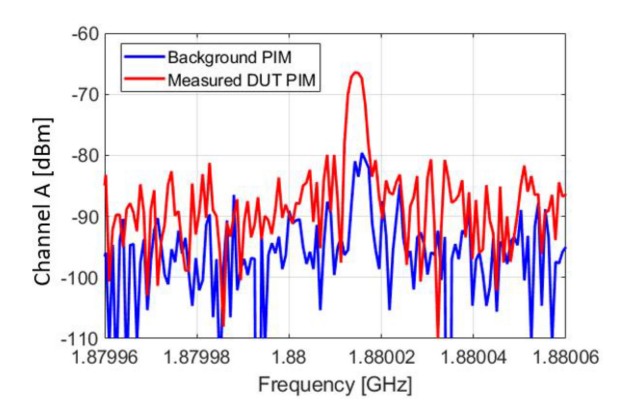


Fig. 6. Comparison between background PIM and measured DUT PIM at  $f_{\rm PIM}=1880.0$  MHz. The SNR is about 15 dB.

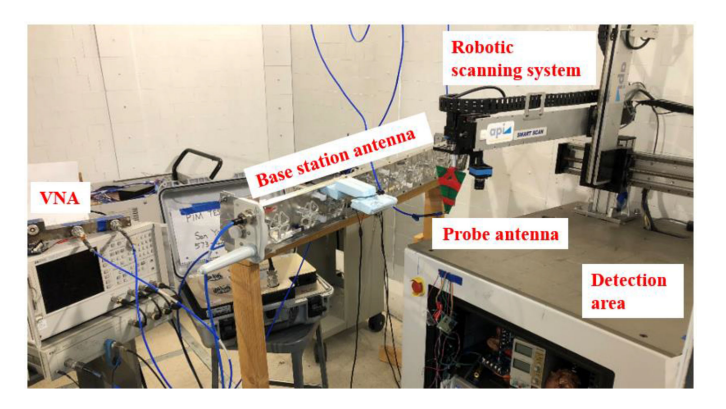


Fig. 7. Uniform sampling ESM setup using a robotic scanning system.

with the help of the filters, and it is referred to as the background PIM signal.

The comparison between the measured DUT PIM and the background PIM is performed for a PIM-generating PCB placed 26 cm beneath the probe antenna in Fig. 6. About 15 dB SNR is achieved for this case, which is considered to be good enough.

Finally, for the purpose of the ESM imaging the complex electromagnetic field amplitude (without the probe correction) for a given orientation of the probe (i.e., a certain component of the field) was reconstructed as  $E=Ae^{j\Delta\varphi}$ , where A is the magnitude of the signal in the VNA channel A, and  $\Delta\varphi$  is the phase difference between the signals in channels A and B.

# IV. UNIFORM SAMPLING ESM APPLICATION

To illustrate the principle of the ESM imaging, uniform sampling was performed using a robotic scanning system (shown in Fig. 7).

The DUT is a PCB at a distance of about 70 cm away from the base station antenna. The probe antenna is set 26 cm above the imaging plane, which is about 1.6 times larger than the wavelength at the PIM frequency of 1.88 GHz ( $\lambda = 16$  cm).

As Fig. 8 shows, the PCB board is placed at a known position (0.2, 0.2 m) in the detection area of the robotic scanner. The DUT plane and the scanning plane have the same size  $(0.3 \times 0.3 \text{ m})$ , and  $7^2$  scanning points are collected uniformly on the scanning plane. The scanning step size is therefore 0.3/7 = 0.043 [m], which is approximately one fourth of the wave length (the step size is selected to satisfy

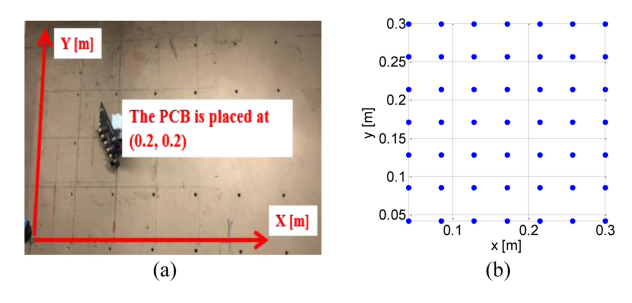


Fig. 8. PIM is generated by a PCB placed at (0.2, 0.2 m) on the (a)  $0.3 \times 0.3 \text{ m}$  image plane;  $7^2$  scanning points are collected unifromly on the (b)  $0.3 \times 0.3 \text{ m}$  scanning plane.

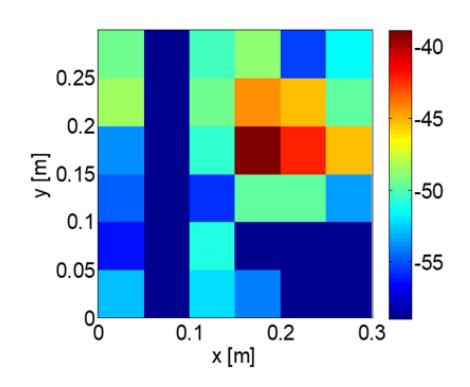


Fig. 9. Reconstructed E-field magnitude in dBV/m when the PCB board placed at  $(0.2,\,0.2~\text{m})$  using uniform sampling ESM.

the Nyquist sampling criterion which usually estimates the maximum spatial frequency of the far-field as  $2/\lambda$ ).

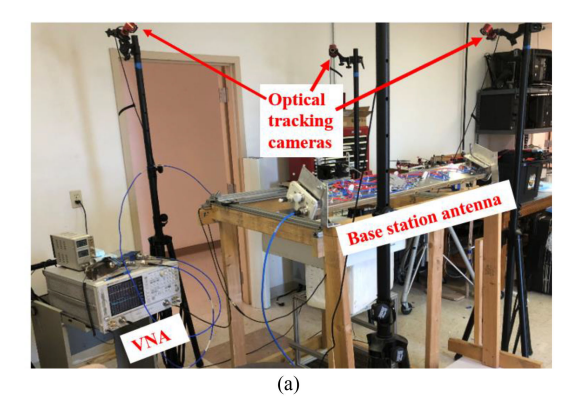
Fig. 9 presents the magnitude of the reconstructed image. The maximum magnitude (the darkest red spot) is found around the known position of the PCB board (0.2, 0.2 m). In case of the uniform sampling ESM, finer measurement grid increases the number of pixels in the reconstructed image and visually helps to identify the radiating sources, but at the expense of longer measurement time. For this case, however, just  $7^2$  scanning points is sufficient to localize the DUT source.

The example shows that uniform ESM can successfully localize a PIM source.

## V. SPARSE SAMPLING ESM APPLICATION

Compared to ESM with uniform sampling, sparse ESM can provide the convenience of manual scanning without using a robotic scanning system. Due to the flexibility of manual scanning, fields value can be selectively obtained based on the real time observation of the reconstructed field strength. The scanning becomes faster and more efficient.

Also, sparse ESM potentially can achieve images with acceptable quality with fewer measurement (compared to the uniform sampling) points [14], [15]. For the sparse ESM a predefined grid of zero values is introduced. The gird is usually defined with a step size that is much smaller than the wavelength to minimize the phase errors in the measured field caused by the differences between the actual and discretely assigned locations of the probe. As the values of the field are obtained by scanning, the grid gets populated and the image is calculated according to (1). As the number of samples increases, the image quality improves and the operator makes a decision to terminate



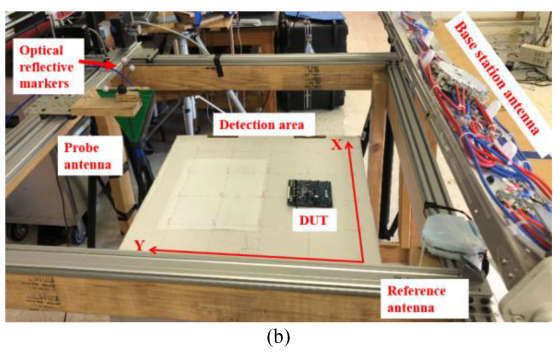


Fig. 10. Sparse sampling ESM setup using an optical tracking system. (a) Optical tracking cameras; (b) detection and scanning area.

scanning if a certain criterion is reached (for example a certain image SNR level is reached) [14].

In the experiments presented below the sparse sampling data is collected by a manual scanner and then the reconstruction is done using the sparse ESM algorithm as described in [14]. Also, to determine the resolution of the sparse ESM measurement, a set of tests are performed by sweeping the spacing between two PIM sources.

The actual measurement setup is illustrated in Fig. 10. Compared to the uniform sampling ESM, the probe antenna is no longer moved by a robotic arm. It is fixed to a manual scanner on a rigid frame, allowing moving the antenna on the scanning plane in an arbitrary way. An optical tracking system [17], [18] is introduced for determining the location of the probe antenna equipped by a reflective marker. The rest of the setup remains the same as the setup used for uniform sampling ESM. Unlike the robotic scanning system used for uniform sampling, which requires setting scanning area width, length, and step size beforehand, manual scanner allows unconstrained probe movement on the scanning plane (within the physical size of the frame).

The PCB used as the DUT is placed at a known position coordinate (0.2, 0.1 m) for verification. The scanning plane is an area of about 0.4  $\times$  0.4 m, and is approximately 0.256 m above the DUT (which is about 1.5 times larger than the wavelength at the PIM frequency of 1.88 GHz  $\lambda=16$  cm). Hundred scanning points are collected arbitrarily on the scanning plane by moving the scanner manually. Fig. 11 shows a typical scanning trajectory.

The reconstructed images with the size of  $0.7 \times 0.7$  m are shown in Fig. 12. The hotspot of the magnitude is found around the known position of the PCB board (0.2, 0.1 m) clearly. Compared to the image reconstructed using uniform sampling ESM shown in Section IV, the increased number of pixels due to high density of the predefined grid helps to identify the emission sources visually.

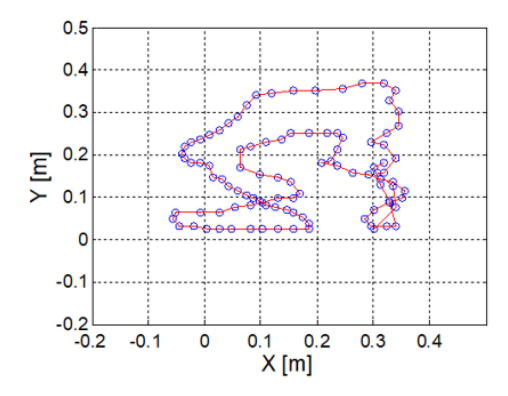


Fig. 11. In the sparse ESM one hunderd scanning points are collected arbitrarily.

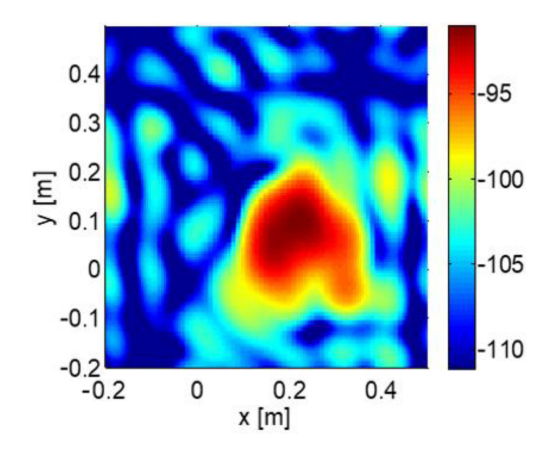


Fig. 12. Reconstructed E-field magnitude in dBV/m when the PCB board placed at (0.2, 0.1 m).

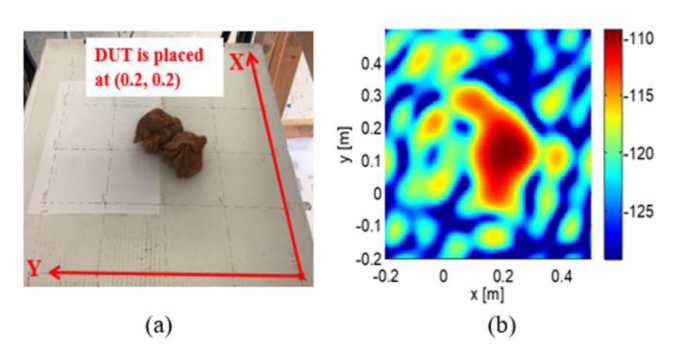


Fig. 13. (a) Photo of the copper wool under test, and (b) reconstructed E-field magnitude in dBV/m.

Another test is performed using a piece of copper wool placed at the position (0.2, 0.2 m) as illustrated in Fig. 13. Compared to the PCB scanned in the previous test, the physical size of the copper wool is larger than the PCB, which leads to a larger red spot. The maximum magnitude (the darkest red spot) is found around the known position of the copper wool.

Investigation on the resolution of the reconstructed image is performed by using two PIM sources (PCBs with nonlinear components). As illustrated in Fig. 14, the spacing between two boards is swept from 30 to 10 cm. The resolution will be defined as the distance at which the sources can no longer be discriminated.

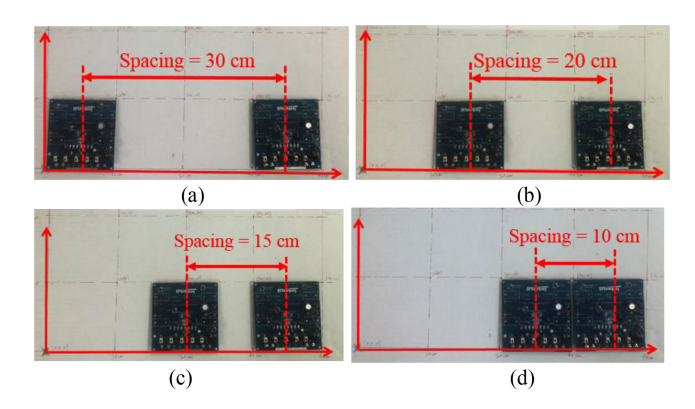


Fig. 14. To determine the resolution of reconstructed E-field, the spacing between two PCBs are swept from 30 to 10 cm: (a) spacing = 30 cm  $(1.9\lambda)$ ; (b) spacing = 20 cm  $(1.3\lambda)$ ; (c) spacing = 15 cm  $(0.9\lambda)$ ; (d) spacing = 10 cm  $(0.6\lambda)$ .

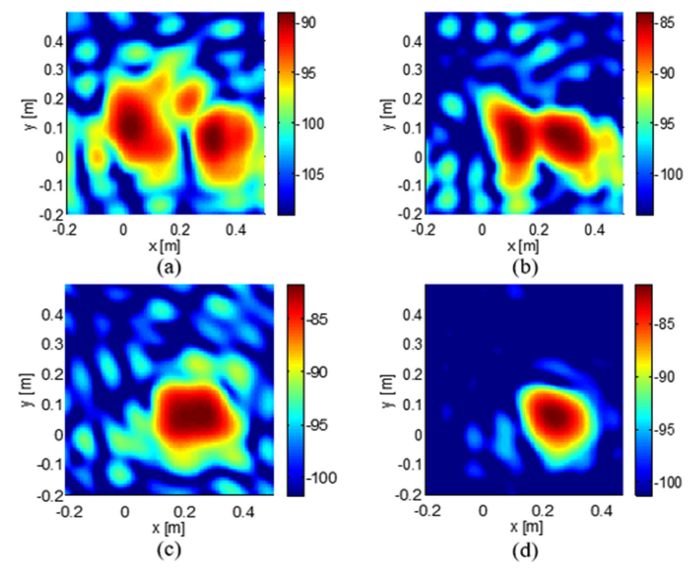


Fig. 15. Reconstructed E-field magnitude in dBV/m of two PCBs with (a) spacing =  $30 \text{ cm } (1.9\lambda)$ ; (b) spacing =  $20 \text{ cm } (1.3\lambda)$ ; (c) spacing =  $15 \text{ cm } (0.9\lambda)$ ; (d) spacing =  $10 \text{ cm } (0.6\lambda)$ .

According to the Fig. 15, two sources can be clearly identified when spacing is larger than 20 cm. They can be barely recognized when the spacing is reduced to 15 cm. Finally, as the spacing reduced to 10 cm two sources become overlapped. Thus, a conservative estimation of the reconstructed ESM image resolution is 15 cm.

The theoretical resolution (R) of the ESM can be calculated using the following equation [13]:

$$R = \frac{\lambda}{2 \cdot NA} \tag{2}$$

where  $\lambda$  is the wavelength, and NA is the numerical aperture of the imaging system. The numerical aperture is in turn related to the refractive index of the medium n and the aperture angle as

$$NA = n \cdot \sin \theta. \tag{3}$$

For our setup with n=1 and  $\theta=38^{\circ}$ , the theoretical resolution is about 13 cm, which agrees well with the value estimated by the measurement (15 cm).

#### VI. CONCLUSION

An ESM-based PIM radiation source localization method has been developed. Using the proposed method, PIM sources can be detected without direct access to the DUT, allowing to detect PIM sources at relatively large distances (several wavelengths). Moreover, the influence of background PIM generated by surrounding environment can be reduced by ESM focusing. Both uniform and sparse ESM strategies can be used. The approach offers an effective PIM source localization solution.

#### REFERENCES

- F. Arazm and F.A. Benson, "Nonlinearities in metal contacts at microwave frequencies," *IEEE Trans. Electromagn. Compat.*, vol. EMC-22, no. 3, pp. 142–149, Aug. 1980.
- [2] X. Chen et al., "Analytic passive intermodulation behavior on the coaxial connector using Monte Carlo approximation," *IEEE Trans. Electromagn.* Compat., vol. 60, no. 5, pp. 1207–1213, Oct. 2018.
- [3] X. Chen and Y. He, "Reconfigurable passive intermodulation behavior on nickel-coated cell array," *IEEE Trans. Electromagn. Compat.*, vol. 59, no. 4, pp. 1027–1034, Aug. 2017.
- [4] S. Yang, W. Wu, S. Xu, Y. Zhang, D. Stutts, and D. Pommerenke, "A passive intermodulation source identification measurement system using a vibration modulation method," *IEEE Trans. Electromagn. Compat.*, vol. 59, no. 6, pp. 1677–1684, May 2017.
- [5] J. R. Wilkerson, I. M. Kilgore, K. G. Gard, and M. B. Steer, "Passive intermodulation distortion in antennas," *Antennas Propag.*, *IEEE Trans.*, vol. 63, no. 2, pp. 474–482, Feb. 2015.
- [6] P. L. Lui and A. D. Rawlins, "Passive non-linearities in antenna systems," in *Proc. IEE Colloq. Passive Intermodulation Products Antennas Related Struct. Tech. Dig.*, London, U.K., Jun. 1989, pp. 6/1–6/7.
- [7] A. Shitvov, A. Schuchinsky, and D. Zelenchuk, "Near-field mapping of passive intermodulation in printed circuits," in *Proc. 4th Eur. Conf. Antennas Propag.*, Barcelona, Spain, 2010, pp. 1–4.
- [8] A. Shitvov, D. Zelenchuk, A. Schuchinsky, and V. Fusco, "Passive intermodulation generation on printed lines: Near-field probing and observations," *IEEE Trans. Microw. Theory Tech.*, vol. 56, no. 12, pp. 3121–3128, Dec. 2008.

- [9] S. Hienonen, V. Golikov, P. Vainikainen, and A. V. Raisanen, "Near-field scanner for the detection of passive intermodulation sources in base station antennas," *IEEE Trans. Electromagn. Compat.*, vol. 46, no. 4, pp. 661–667, Nov. 2004.
- [10] T. Bell, J. Nankivell, "White paper Range to fault technology," Kaelus Inc., 2017. [Online]. Available: https://www.kaelus.com/getmedia/50f422f9-9ced-4149-983d-51a0fd9348d3/Range-to-Fault-Technology. pdf.aspx?ext=.pdf, Accessed: Sep. 2019.
- [11] Anritsu Company, "Using distance-to-PIM (DTP) and distance-to-fault (DTF) trace overlay to speed site repair," 2015. [Online]. Available: https://dl.cdn-anritsu.com/en-us/test-measurement/files/Application-Notes/Application-Note/11410-00869A.pdf, Accessed: Sep. 2019.
- [12] H. Yang, H. Wen, Y. Qi, and J. Fan, "An equivalent circuit model to analyze passive intermodulation of loose contact coaxial connectors," *IEEE Trans. Electromagn. Compat.*, vol. 60, no. 5, pp. 1180–1198, Feb. 2018.
- [13] P. Maheshwari, H. Kajbaf, V. V. Khilkevich, and D. Pommerenke, "Emission source microscopy technique for EMI source localization," *IEEE Trans. Electromagn. Compat.*, vol. 58, no. 3, pp. 729–737, Jun. 2016.
- [14] L. Zhang et al., "Sparse emission source microscopy for rapid emission source imaging," *IEEE Trans. Electromagn. Compat.*, vol. 59, no. 2, pp. 729–737, Apr. 2017.
- [15] M. Sørensen, H. Kajbaf, V. Khilkevich, L. Zhang, and D. Pommerneke, "Analysis of the effect on image quality of different scanning point selection methods in sparse ESM," *IEEE Trans. Electromagn. Compat.*, Early Access, Sep. 2018.
- [16] 2018CCI PIMPro1921. [Online]. Available: http://www.cciproducts.org/ www2/index.php/products/pim-analyzers/pimpro-rack-mount/item/296, Accessed: Sep. 2019.
- [17] Optical tracking system. [Online]. Available: https://optitrack.com/ products/flex-13/, Accessed: Sep. 2019.
- [18] H. He, V. Khilkevich, and D. Pommerenke, "2D imaging system with optical tracking for EMI source localization," in *Proc. IEEE Symp. Elec*tromagn. Compat. Signal Integrity, Santa Clara, CA, USA. May 2015, pp. 107–110.